Monthly Notices of the ROYAL ASTRONOMICAL SOCIETY

MNRAS **520,** 4134–4146 (2023) https://doi.org/10.1093/mnras/stad420
Advance Access publication 2023 February 7

First on-sky demonstration of a scintillation correction technique using tomographic wavefront sensing

Kathryn E. Hartley ,★ Oliver J. D. Farley , Matthew J. Townson , James Osborn and R. W. Wilson
Centre for Advanced Instrumentation, Department of Physics, University of Durham, South Road, Durham, DH1 3LE, UK

Accepted 2023 February 2. Received 2023 February 2; in original form 2022 October 25

ABSTRACT

Scintillation noise significantly limits high precision ground-based photometry of bright stars. In this paper, we present the first ever on-sky demonstration of scintillation correction. The technique uses tomographic wavefront sensing to estimate the spatial-temporal intensity fluctuations induced by high altitude optical turbulence. With an estimate of the altitudes and relative strengths of the turbulent layers above the telescope, the wavefront sensor data from multiple guide stars can be combined to estimate the phase aberrations of the wavefront at each altitude through the use of a tomographic algorithm. This 3D model of the phase aberrations can then be used to estimate the intensity fluctuations across the telescope pupil via Fresnel propagation. The measured photometric data for a given target within the field of view can then be corrected for the effects of scintillation using this estimate in post-processing. A simple proof-of-concept experiment using a wavefront sensor and a stereo-SCIDAR turbulence profiler attached to the 2.5 m Isaac Newton Telescope was performed for a range of exposure times using the Orion Trapezium cluster as the reference stars. The results from this on-sky demonstration as well as simulations estimating the expected performance for a full tomographic AO system with laser guide stars are presented. On-sky, the scintillation index was reduced on average by a factor of 1.9, with a peak of 3.4. For a full tomographic system, we expect to achieve a maximum reduction in the scintillation index by a factor of ∼25.

Key words: atmospheric effects – instrumentation: adaptive optics – methods: observational – techniques: photometric.

1 INTRODUCTION

High precision ground-based photometry is vital for a range of studies that look for small intrinsic variations in the intensity of astronomical sources. These include observations of exoplanet transits, variable stars, and stellar seismology. However, such observations can be significantly limited by the effects of the Earth's atmosphere. As the light from an astronomical source passes through the atmosphere, high altitude regions of optical turbulence produce spatial intensity fluctuations across the telescope pupil. These spatial intensity patterns change over time as the turbulence evolves and translates with the wind (Dravins et al. 1997a). This results in photometric noise known as scintillation which can be seen by the naked eye as the twinkling of the stars. For large telescopes, these intensity variations can be on the scale of ∼ 0.1 to ∼ 1 per cent (Osborn et al. 2015) averaged over exposures of a few seconds for time-resolved photometry. This significantly limits the ability to measure intrinsic variations of bright objects on short time-scales.

For bright stars, scintillation is the dominant noise source, the observations are scintillation limited (Föhring et al. 2015). Hence, if this noise can be corrected, very high-precision ground-based photometry could be achieved, greatly enhancing research such as the study of multispectral photometry of exoplanet transits used to determine the composition of the exoplanet's atmosphere (Madhusudhan et al. 2014). Atmospheric scintillation correction could also lead to new avenues of research.

However, correcting scintillation noise is a significant challenge. As it is produced by high altitude turbulence, the range of angles over which it is correlated is very small (Kornilov 2012). Therefore, it cannot be corrected directly through differential photometry as the probability of having a bright star within the isophotometric angle is small. Several scintillation correction techniques have been proposed including conjugate plane photometry (Osborn et al. 2011) and differencing signals from binary stars (Ryan & Sandler 1998), although currently no such technique is in common practice.

Osborn (2014) proposed a new scintillation correction technique for large telescopes, that uses the Wavefront Sensor (WFS) data from multiple guide stars near the astronomical source of interest to tomographically reconstruct the phase aberrations above the telescope. This 3D model of the phase can be used in simulation with Fresnel propagation to produce an estimate for the scintillation pattern across the telescope pupil. This estimated scintillation pattern can then be used to correct the measured photometric data for the fluctuations due to scintillation. The model can be used to correct the scintillation in any direction within the field of view (FOV) and at any wavelength and thus all objects within the field can be corrected simultaneously.

A significant advantage of this proposed method is that, if desired, the numerical scintillation correction can be applied using the wavefront sensors of any existing tomographic Adaptive Optics (AO) systems without the need for any additional instrumentation.

★ E-mail: kathryn.e.hartley@durham.ac.uk

In addition, this technique can be applied entirely in post-processing and can therefore be optimized for any observation. Only the WFS data and an estimate for the turbulence profile are required to perform the scintillation correction, no real time adaptive optical correction is needed. In addition, a separate turbulence profiler is not necessarily needed as the turbulence profile can be estimated from the telemetry data.

In this paper, we present the first on-sky demonstration of a scintillation correction technique on the Isaac Newton Telescope (INT), ING, La Palma, Spain, using three stars from the Orion Trapezium cluster as the tomographic reference stars. A single WFS was used to measure the optical phase aberrations for all three stars and a SCIDAR (Shepherd et al. 2013) instrument was used to estimate the turbulence profile. A Multi Conjugate Adaptive Optics (MCAO) tomographic algorithm (Fusco et al. 2001) detailed in Section 2.2 was used to perform the tomographic reconstruction in post-processing.

Section 2 describes the scintillation phenomenon and the tomographic algorithm used. Section 3 details the data acquisition and in Section 4, the data reduction techniques used in this demonstration are discussed. In Section 5, the on-sky results are presented and compared to simulations. In Section 6, we present the results from a simulation of a full tomographic AO system on the Very Large Telescope (VLT). Finally, these results are discussed and concluded in Section 7.

2 THEORY

2.1 Scintillation noise

The general theory for ground based scintillation was developed by Tatarski (1967) and has been expanded upon by Roddier (1981) and Young (1969). Extensive studies have been carried out by Mikesell (1955), Dainty et al. (1982) and more recently Dravins et al. (1997a, b, 1998) who looked at the impact of wavelength and telescope aperture on the scintillation noise measured.

Optical turbulence can focus or defocus the incoming starlight leading to 'flying shadows' crossing the telescope pupil. The temporal fluctuations occur both because the 'flying shadow' patterns are moving with the wind but are also intrinsically changing themselves (Dravins et al. 1997a). In most modelling, Taylor's 'frozen flow' is assumed as the time taken for the patterns to cross the telescope pupil is less than the time taken for the turbulence to evolve (Taylor 1938).

Since scintillation is an effect of optical propagation, it is mainly caused by turbulence in the upper troposphere. This was confirmed empirically by Mikesell in 1955 in which he used lamps on high altitude balloons to simulate artificial stars (Mikesell 1955). The scintillation measured for these artificial stars were less than that of the adjacent real stars, suggesting scintillation originates from turbulence at higher altitudes. It is for this reason that good photometric conditions can be observed during bad seeing; the angular seeing results from the strongest turbulence layer which is often much closer to the ground (Osborn et al. 2010) whilst scintillation is produced by turbulence in the upper atmosphere. Consequently, comparison stars cannot ordinarily be used to correct for scintillation as the coherence angle (i.e. the isophotometric) will be much smaller than the expected star separation.

The level of scintillation is quantified by the scintillation index σ_I^2. This is given by the variance of the relative intensity fluctuations:

$$\sigma_I^2 = \frac{\langle I^2 \rangle - \langle I \rangle^2}{\langle I \rangle^2}, \tag{1}$$

where I is the intensity as a function of time and $\langle \cdot \rangle$ represents an ensemble average. Using the normalized intensity ensures that the scintillation index does not depend on the magnitude of the star and therefore represents only the strength of atmospheric scintillation. The scintillation rms (root-mean-sqaure) fractional noise, σ_I, is then the square root of the scintillation index. Scintillation can therefore be studied either by measuring the scintillation index or the direct scintillation patterns (Dravins et al. 1997a). The theoretical scintillation index is given by the integral of the scintillation power spectrum defined by Kornilov (2012).

For telescopes with $D \gg r_f$, where r_f is the Fresnel radius ($r_f = \sqrt{\lambda z}$), the scintillation index for short exposures can be estimated as (Sasiela 2012):

$$\sigma_I^2 = 17.34 D^{-7/3} (\cos(\gamma))^{-3} \int_0^\infty h^2 C_n^2(h) \mathrm{d}h, \tag{2}$$

where D is the telescope aperture diameter, h is the altitude of the turbulent layer, $C_n^2(h)$ is the refractive index structure constant (a measure of the vertical profile of the turbulence strength), and γ is the zenith angle.

For long exposure times, defined as $t \gg t_{\mathrm{cross}}$, where t_{cross} is the time taken for the turbulent layer to cross the telescope pupil, the scintillation index is given by (Sasiela 2012):

$$\sigma_I^2 = 10.66 D^{-4/3} t^{-1} (\cos(\gamma))^{\alpha} \int_0^\infty \frac{h^2 C_n^2(h)}{V_\perp(h)} \mathrm{d}h, \tag{3}$$

where t is the exposure time, α is the exponent of the airmass, and $V_\perp(h)$ is the wind velocity profile. The value of α depends on the wind direction and will be -3 when the wind is transverse to the azimuthal angle of the star and -4 when it is longitudinal.

From the above equations, it can be seen that as the telescope aperture and exposure time increase, scintillation noise decreases proportional to $D^{-4/3}t^{-1}$. On the other hand, shot noise is proportional to $D^{-2}t^{-1}$, hence as the telescope aperture is increased, scintillation noise dominates. Scintillation correction is therefore more significant for large telescopes.

2.2 MCAO tomography

To perform the scintillation correction technique, a tomographic reconstruction algorithm is required. MCAO was initially proposed by Beckers in 1988 (Beckers 1988) to increase the field of view of AO systems. It works by stacking several deformable mirrors (DMs) in a series which are optically conjugated to the whole turbulent volume. A tomographic reconstruction algorithm is used to produce a 3D model of the turbulent volume above the telescope from the WFS measurements. The AO correction for each layer can then be applied to its respective DM. See Fig. 1 for a schematic demonstrating this technique. This 3D model of the phase aberrations can also then be used to correct for the scintillation noise. This is done by propagating the reconstructed phase to the ground, in simulation, to produce an estimate for the scintillation pattern.

The tomographic algorithm used in this paper was developed by Fusco et al. (2001) and uses a minimum-mean-square-error (MMSE) estimator that minimises the mean residual phase variance in the FOV of interest. The basis of this model is outlined as follows.

The atmosphere can be modelled as a discrete sum of turbulent layers located at different heights (Roddier 1981). Hence, the total optical phase aberration seen across the telescope pupil for direction

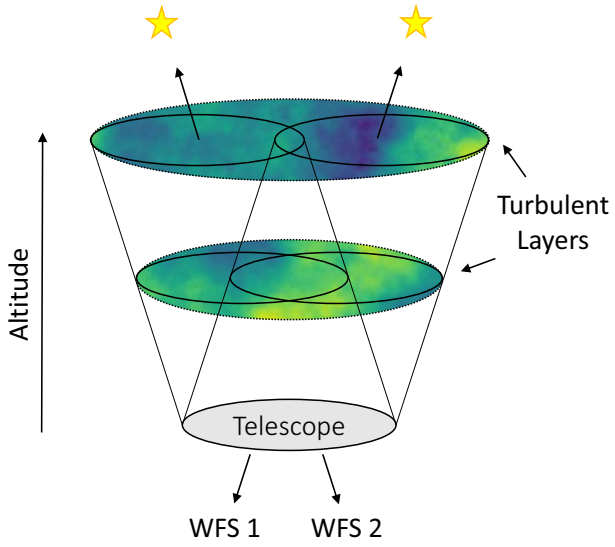

Figure 1. A schematic showing the concept of MCAO. Multiple WFS probe the turbulent atmosphere and a DM is conjugated to each turbulent layer.

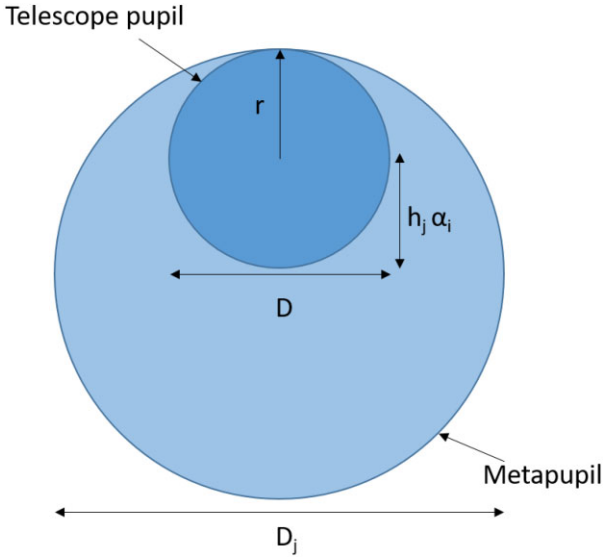

Figure 2. A schematic showing the de-centered part of the meta-pupil at altitude h_j seen by the WFS in direction $\boldsymbol{\alpha_i}$.

$\boldsymbol{\alpha}$ in the near field approximation can be given as:

$$\Phi(\boldsymbol{r}, \boldsymbol{\alpha}) = \sum_{j=1}^{N_t} \phi_j(\boldsymbol{r} + h_j\boldsymbol{\alpha}), \tag{4}$$

where $\boldsymbol{r}$ is the pupil coordinate, N_t is the number of turbulent layers, and h_j is the height of the jth layer.

The wavefront sensor measurements are assumed to be perfect except for an additional noise term. The measured phase for direction $\boldsymbol{\alpha_i}$ is then given by:

$$\Phi^m(\boldsymbol{r}, \boldsymbol{\alpha_i}) = \sum_{j=1}^{N_t} \phi_j(\boldsymbol{r} + h_j\boldsymbol{\alpha_i}) + n_i(\boldsymbol{r}), \tag{5}$$

where $n_i(\boldsymbol{r})$ is the noise in the WFS measurement which is assumed to have a Gaussian distribution. The reconstructed phase is then:

$$\hat{\Phi}(\boldsymbol{r}, \boldsymbol{\alpha}) = \sum_{k=1}^{N_{\rm DM}} \hat{\phi}_k(\boldsymbol{r} + h_k\boldsymbol{\alpha}), \tag{6}$$

where h_k are the altitudes of the conjugated DMs.

The reconstruction matrix is the matrix, $\mathbf{W}$, that fulfils the following equation:

$$\hat{\boldsymbol{\phi}} = \mathbf{W}\boldsymbol{\Phi}^m. \tag{7}$$

In this paper, the model approximation (MA) is used in which it is assumed that all the turbulence is located on the DMs. In this case, the turbulence profile is modelled by a small number of turbulent layers called equivalent layers (ELs). The EL positions and strength are calculated by sampling the C_n^2 profile into N_{EL} slabs. In this case, the MMSE solution for the reconstructed matrix is given by:

$$\mathbf{W_{MA}} = \mathbf{C_\phi}(\mathbf{M}_{\mathbf{N_{GS}}}^{\mathbf{N_{EL}}})^{\rm T}[\mathbf{M}_{\mathbf{N_{GS}}}^{\mathbf{N_{EL}}}\mathbf{C_\phi}(\mathbf{M}_{\mathbf{N_{GS}}}^{\mathbf{N_{EL}}})^{\rm T} + \mathbf{C}_n]^{-1}. \tag{8}$$

where $+$ and T denote the generalized pseudo inverse and the transpose, respectively and where $\mathbf{C_\phi}$ and $\mathbf{C_n}$ are the turbulence and noise covariance matrices and where $\mathbf{M}_{\mathbf{N_{GS}}}^{\mathbf{N_{EL}}}$ is a matrix which projects the guide star measurements onto the ELs.

In the Zernike basis, $\boldsymbol{\phi}$ and $\hat{\boldsymbol{\phi}}$ are simply vectors of Zernike coefficients. $\mathbf{C_\phi}$ is the Zernike–Kolmogorov turbulence covariance matrix given by Noll (1976) and $\mathbf{C_n}$ is the noise covariance matrix given by Rigaut & Gendron (1992). In addition, $\mathbf{M}_{\mathbf{N_{GS}}}^{\mathbf{N_{EL}}}$ is a matrix that consists of the decomposition of the decentred Zernike polynomials $[Z_{l,j}(\boldsymbol{r} + h_j\boldsymbol{\alpha})]$ on to a Zernike basis defined on the telescope pupil (see Fig. 2). A full description of this matrix is given by Ragazzoni, Marchetti & Rigaut (1999).

2.3 Scintillation correction

As shown in Section 2.2, if the altitudes and relative strengths of the turbulent layers are known, the WFS data from multiple guide stars can be used to produce a 3D model of the instantaneous phase aberrations above the telescope in the Zernike basis. These reconstructed phase aberrations can be used with Fresnel propagation to compute an estimate for the spatial intensity fluctuations across the pupil for each frame. Integrating the estimated spatial scintillation pattern for each frame gives the estimated intensity. This estimate of the intensity can then be used to normalize the measured photometry.

Large metapupils at each reconstructed layer are needed for the scintillation estimation. This is due to the Fresnel propagation producing diffraction rings at the edge of the propagated pupil. Hence, a pupil larger than the telescope aperture is used in the Fresnel propagation to produce a reconstructed scintillation pattern over a larger area from which the telescope pupil can be cut out. This prevents the addition of significant noise from the diffraction rings at the edge of the reconstructed scintillation pattern.

Since scintillation is produced by the high altitude turbulence, only the high altitude reconstructed layers need to be propagated. Fortunately, since the metapupil size is proportional to the altitude, as shown in Figs 1 and 2, the reconstructed layers of interest are over large metapupils.

The wavefront sensor effectively acts as a low-pass spatial filter such that only low-order phase aberrations are measured. Since the time-scale of the intensity fluctuations is determined by the spatial scale and wind speed associated with the high-altitude turbulence. Therefore, only the low temporal frequency intensity variations can be corrected.

The application of tomographic wavefront sensing for scintillation noise correction places different requirements on the asterism scale.

This is because scintillation is produced by only high-altitude turbulence. At higher altitudes there is less overlap between the WFS measurements, as seen in Fig. 1. The altitude at which the guide star measurements no longer overlap is given by $h_{\max} = \frac{D}{\theta}$, where D is the telescope diameter and θ is the angle between the guide stars. Hence, for scintillation correction, the stars must be much closer to one another than is required for traditional AO (where the ground layer is often the dominant source), in order to provide good sampling of these high layers. As such, this method is better for large telescopes, where the higher layers are better sampled. Turbulent layers above the altitude at which the WFS measurements no longer overlap will not be sampled and will add noise to the tomographic reconstruction.

Since compact asterisms are required, the sky coverage for scintillation correction using Natural Guide Stars (NGS), is severely limited, with most targets of interest not having sufficiently bright stars nearby to perform the correction. Hence, in practice, this technique requires Laser Guide Stars (LGS), a technology becoming more prevalent at telescope sites.

However, a key benefit to this method is that it can be easily applied to any existing LGS tomographic AO system. The latest large and extremely large telescopes will all be equipped with tomographic AO systems, such as the MORFEO (Ciliegi 2021) and HARMONI (Thatte et al. 2010) for the ELT, which are ideal bases for this scintillation correction technique. The instrumentation could be set up to apply the scintillation correction in real time, or it can be applied entirely in post-processing using the WFS telemetry and the profile from WFS data. Correction in post-processing is ideal as the data reduction can be optimized for each observation and, so long as regular turbulence profiling is done, the tomographic reconstruction matrix can be updated as regularly as necessary.

2.4 Simulation

To investigate this technique, a numerical simulation was developed using the SOAPY (Reeves 2016) and AOTOOLS (Townson et al. 2019) PYTHON packages. This simulation used a phase screen Monte Carlo representation of atmosphere. The vertical optical turbulence profiles were based on SCIDAR observations at La Palma and Paranal (Farley et al. 2018). Fresnel propagation of the phase screens was used to produce an intensity fluctuation pattern for each exposure. For all the simulations presented, a WFS that includes the random measurement errors due to shot noise, but otherwise perfectly measures the atmospheric Zernike terms, was simulated for each star. The WFS noise model used is given by Wilson & Jenkins (1996). The Zernike modes are measured directly without modelling the centroid calculation and modal reconstruction processes.

The tomographic reconstruction algorithm described in Section 2.2 was produced assuming perfect knowledge of the turbulent layer altitudes and relative strengths. The number of layers used in each simulation was dependent on the telescope scale. For the INT simulations, 15 layer atmospheres were simulated which were represented by 5 layers in the reconstruction matrix thus including some fitting error. However, for the VLT simulations, to save computational time, 5 layer atmospheres were simulated with an equal number of layers used in the tomographic reconstruction matrix thus giving an upper limit in the correction that can be achieved.

The reconstruction matrix was applied to the simulated WFS measurements to get the reconstructed phase aberrations at each altitude. The same number of Zernike modes was used for each metapupil. The reconstructed phase was used with Fresnel propagation to produce an estimate for the intensity fluctuation pattern for each exposure. The Fresnel propagation was performed using the angular spectrum function in AOTOOLS (Townson et al. 2019). Details of this method are given in Schmidt (2010). This estimated intensity was then used to correct the measured intensity.

This numerical simulation was used to investigate the impact of multiple parameters on the scintillation correction achieved and to find a suitable target for the on-sky experiment. In addition, Section 6 uses this simulation to explore the limitations of this technique and the expected performance for an LGS tomographic wavefront sensing facility on a large (8m) telescope.

2.5 Performance metrics

The performance of the correction technique is determined by measuring the Pearson r correlation coefficient between the measured intensity and the tomographically reconstructed intensity. The Pearson r coefficient measured between two variables x and y is given by:

$$r = \frac{\sum(x_i - \bar{x})(y_i - \bar{y})}{\sqrt{\sum(x_i - \bar{x})^2 \sum(y_i - \bar{y})^2}}, \tag{9}$$

which is equivalent to:

$$\mathrm{Cor}(x, y) = \frac{\mathrm{Cov}(x, y)}{\sqrt{\sigma_x^2 \sigma_y^2}}, \tag{10}$$

where $\mathrm{Cov}(x, y)$ is the covariance between x and y.

In addition, the performance is also measured in terms of the 'scintillation correction factor' which is the factor by which the scintillation index has been reduced. The reduction in the measured scintillation index that can be expected is directly related to the correlation coefficient measured between the measured photometry and the reconstructed intensity.

The corrected light curve will have a measured variance of:

$$\begin{aligned} \langle |I - I_r|^2 \rangle &= \langle I \rangle^2 + \langle I_r \rangle^2 - 2\langle I, I_r \rangle \\ &= \sigma_I^2 + \sigma_{I_r}^2 - 2\mathrm{Cov}(I, I_r), \end{aligned} \tag{11}$$

where I is the measured intensity and I_r is the reconstructed intensity. If we assume that $\sigma_I^2 \approx \sigma_{I_r}^2$, then:

$$\langle |I - I_r|^2 \rangle = 2(\sigma_I^2 - \mathrm{Cov}(I, I_r)). \tag{12}$$

The scintillation correction factor, which we define as C_{scint}, is given by:

$$C_{\mathrm{scint}} = \frac{\sigma_I^2}{\sigma_{|I - I_r|}^2}, \tag{13}$$

which is equivalent to:

$$C_{\mathrm{scint}} = \frac{\sigma_I^2}{2(\sigma_I^2 - \mathrm{Cov}(I, I_r))} = \frac{1}{2(1 - \mathrm{Cor}(I, I_r))}. \tag{14}$$

The correlation coefficient and the scintillation correction factor are the metrics used to measure the performance of this technique. To achieve any correction in scintillation noise a correlation coefficient of greater than 0.5 is required. In order to halve the scintillation rms noise, a scintillation correction factor of 4 is needed and thus a correlation coefficient of 0.875 is required. Fig 13 shows the relationship between the scintillation correction factor and correlation coefficient helping to visualize the coefficient correlation required for scintillation correction levels. It also indicates the effect of noise on the data reduction optimization as discussed in Section 5.3.

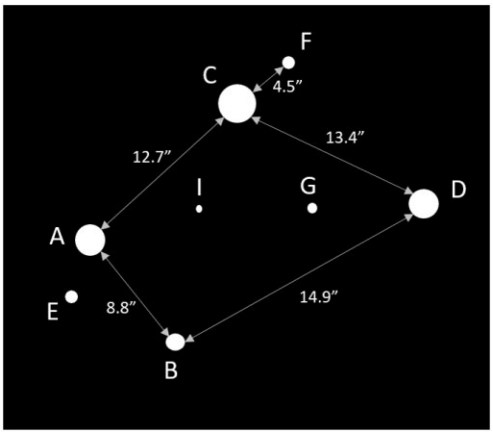

Figure 3. A schematic showing the Orion Trapezium Cluster. Each label defines the name of the star, with Theta-1 Orionis A given by label A, Theta-1 Orionis B given by label B and Theta-1 Orionis C given by label C, etc. The stars used to perform the tomography are Orionis A, C, and D.

3 ON-SKY EXPERIMENT

3.1 Target

Prior to the observing run, a detailed simulation was produced to investigate the scintillation correction technique described in 2.3 and to determine the expected performance on sky. This was used to determine the optimum parameters, such as the best exposure time, and to find a suitable on-sky target. The relatively small aperture size of the INT (2.54 m) severely limited the sky coverage for this demonstration using NGS wavefront sensing. A minimum of three stars are required to perform the tomography, and for sufficient overlap at high altitudes, the stars could only be separated by up to 26 arcsec. In addition, the stars needed to be bright, ideally with V magnitude below 10. One of the three stars must be a scintillation limited star to act as the target. It was found that in order to fully sample the layers in the Zernike basis, the stars needed to be configured in a triangle – a line of stars was found to achieve low performance. Based on these stringent criteria, only three suitable asterisms were found, with the Orion Trapezium (M42) cluster being the optimum and is a favourite target amongst tomography demonstrations (Marchetti et al. 2007).

Fig. 3 shows a diagram of the Orion Trapezium Cluster. To perform the tomography, only three stars from this cluster were used. Theta-1 Orionis A, D, and C were used to perform the tomography and Theta-1 Orionis C, the brightest star with a V magnitude of 5.1, was used as the target.

As can be seen in Fig. 3, there is a faint companion star next to Theta-1 Orionis C labelled as F. This faint star, V = 10.2, can also be seen in the WFS data. Due to its close proximity to the target star, it is included in the aperture photometry. Hence, some noise is introduced. However, this star is significantly fainter than the target star and hence any noise addition will be small.

This asterism was tested in simulation on 15 SCIDAR turbulence profiles that had been previously observed in La Palma (Farley et al. 2018). On average, a good correction factor in the scintillation rms noise of 3.2 was measured.

3.2 Data acquisition

The data presented in this paper were recorded on the 19th of September, 2021 using the INT at the Roque de los Muchachos Observatory in La Palma. This proof of concept experiment was designed with a single WFS and stereo-SCIDAR turbulence profiler attached to the INT. The single 10 x 10 WFS was used to measure the wavefront aberrations for all three of the stars in each direction. The WFS data was also used to perform the aperture photometry. This greatly simplified the data acquisition as only a single camera was needed to collect all of the tomographic and photometric data and ensured the two were synchronized. Fig. 4 shows a photograph of the SCIDAR and WFS instruments attached to the INT. The SCIDAR measurements and WFS data measurements were taken in succession with the reflecting prism at label A used to switch between the two instruments. Hence, the profiling and WFS measurements were not taken simultaneously.

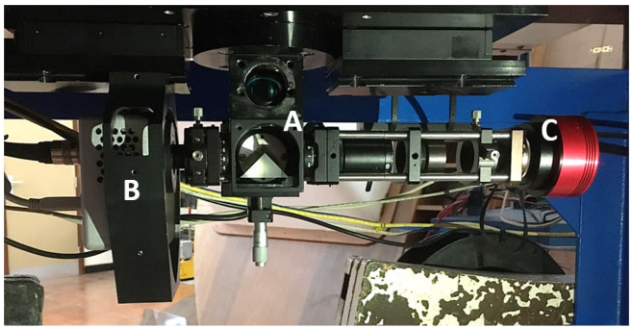

Figure 4. A photo of the instruments connected to the INT. Label A shows the prism that is used to move form one instrument to the other, label B shows the SCIDAR instrument and label C shows the WFS optics and detector.

The WFS optics comprised of a collimating lens, V band filter and a lenslet array, and a detector. A ZWO ASI 1600 MM camera was chosen as a suitable detector for the WFS frames due to the CMOS camera's large format, meaning all the stars WFS data can be encompassed, and fast readout with low readout noise meant that short exposure times could be used. The photometric performance of the camera is also of good standard although it was found that the bias level varied from frame to frame. Hence, a bias level was measured and subtracted for each frame.

At this time of year, the Trapezium Cluster did not rise until early in the morning, reaching an altitude of 40 deg around 5:30 am. Hence, the observations were taken at a low elevation angle. Throughout the observations, the Trapezium was rising and thus changes in airmass added systematic trends to the photometry.

In simulation, it was found that the technique works well using exposure times much longer than typical AO correction. This is because both the wavefront measurements and intensity fluctuations average over time in the same way. Therefore, temporally averaging the wavefront measurement does not bias the reconstructed intensities as both of these are linear processes. Hence, good correction can still be achieved with longer exposure times so long as the temporal fluctuations remain detectable. In addition, because we are performing in post-processing and open loop, we do not need to use a very short exposure time. A range of exposure times was used to investigate the correction performance as a function of exposure time used. The WFS data were collected in contiguous data packets of 50 frames with exposure times of 0.01, 0.1, and 1 s. In simulation, a 0.1 s exposure time resulted in the highest scintillation correction. This can be understood by considering the power spectrum of the intensity fluctuations and is discussed further in Section 5.4.

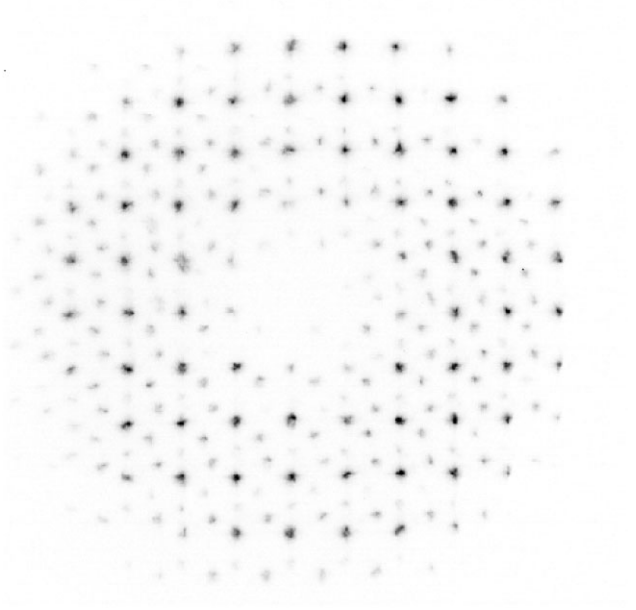

Figure 5. Example of a 0.1 s WFS frame. The colours have been inverted and a maximum pixel value set such that the fainter stars can be more easily seen.

4 DATA REDUCTION

There are multiple steps to performing the data reduction which are outlined below. Each step was optimized to achieve the best performance.

(i) The centroids for each of the three stars of interest are measured from the WFS data.
(ii) The aperture photometry of the target star is measured from the WFS frames.
(iii) The measured star centroids are converted to Zernike modes using a Zernike decomposition matrix.
(iv) The SCIDAR data are used to estimate the turbulence profile and an optimal grouping method (Saxenhuber et al. 2017) is used to compress the profile to fewer layers.
(v) The tomographic reconstruction matrix is produced using the estimated turbulence profile and star cluster geometry and is applied to the measured Zernike slopes to get the reconstructed phase at each altitude.
(vi) The reconstructed phase is used in simulation with Fresnel propagation to produce an estimate for the scintillation pattern across the telescope pupil.
(vii) The measured target light curve is normalized using the summed estimated scintillation patterns and the correlation coefficient and scintillation correction factor are measured.

In this section, each step in the data reduction pipeline is given in more detail with information on the optimization performed for each step.

4.1 Centroiding

The use of a single WFS to measure the spot centroids for all three stars, whilst greatly simplifying the data acquisition, created more challenges for measuring the centroids and performing the aperture photometry. Fig. 5 shows an example image of a 0.1 s WFS frame. As can be seen, the image produced by each subaperture is crowded, with 4 stars in each. As such, windowing was required to prevent contamination from neighbouring stars and masking was used.

The target star is significantly brighter than the companion stars and if it strays into the window of the neighbouring star, its intensity significantly skews the measured centroid. As such, once the centroids of the target star had been measured, a mask was applied to each frame to block out the light of the target star for each subaperture, thus reducing contamination from the target star in measuring the centroids for the other fainter stars.

The Centre of Gravity (CoG) method was used with optimal windowing and thresholding. The optimization was performed by maximizing the scintillation correction performance. Each subaperture had a width of 42 pixels. A window centred on the average subaperture position of each star was used. A window of 18 x 18 pixels for the brighter target star and 16 x 16 pixels for the companion stars was found to be optimal, with a threshold of 0.4. In total, 75 subapertures were used in the tomographic reconstruction. Table 1 shows the average photomertic SNR measured for over all subapertures for each exposure time.

Table 1. A table of the average photometric SNR measured for the target star in each subaperture for each exposure time.

Exposure time	0.02 s	0.1 s	1 s
Measured SNR	13	21	50

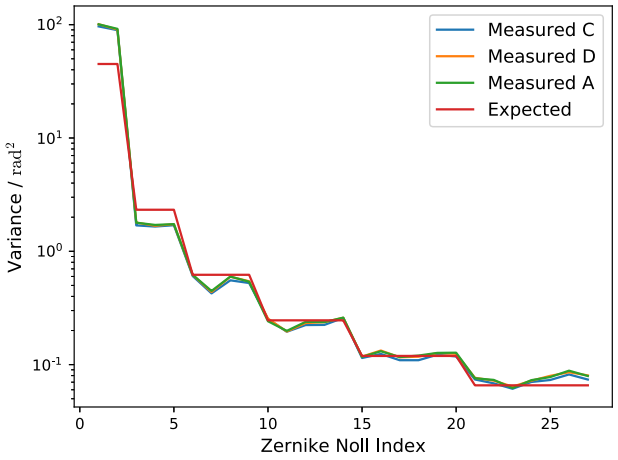

Figure 6. The measured Zernike mode variance for Theta-1 Orionis C, D, and A. The expected variance for $r_0 = 0.16$ m is also plotted.

4.2 Zernike decomposition

Converting the centroids to Zernike modes was done using a Zernike decomposition matrix. As can be seen in Fig. 6, the measured variance of the reconstructed Zernike modes across the telescope aperture for each star closely follows the expected Kolmogorov variance for $r_0 = 0.16$ m measured from the SCIDAR profiles (Noll 1976). This suggests that the Zernike decomposition (Dai 1996) has been implemented accurately and that the average r_0 value has not changed significantly over the data run. The difference in step for order 1 and 2 is likely due to tracking errors.

Since scintillation noise is produced by the low order spherical modes of the incoming wavefront in high-turbulent layers, the most significant modes that need to be measured are the low-order focal and de-focal modes. Fig. 6 shows that the atmospheric phase variance

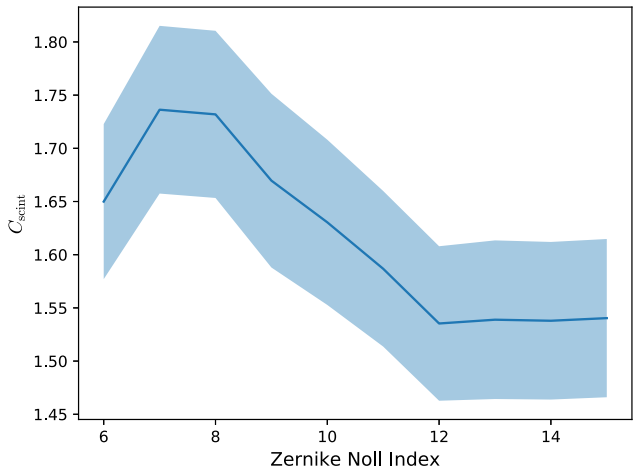

Figure 7. The average measured scintillation correction factor as a function of the Noll index for the 0.1 s data packets. A peak around 8 modes suggest that only low orders are required for the scintillation correction.

associated with low-order modes is much greater than for higher order modes, as expected. Using higher order modes adds noise to the reconstruction whilst providing little additional atmospheric correction.

The number of Zernike modes used in the tomographic reconstruction matrix was optimized for each individual data packet by finding the maximum scintillation correction as a function of the number of modes used to perform the correction. All the layers were reconstructed with the same number of Zernike modes. The average measured scintillation correction factor as a function of the Noll index for the 0.1 s data packets is shown in Fig. 7. A peak around 8 modes is seen. Including higher orders in the reconstruction matrix reduces the scintillation correction factor achieved. This suggests that only low orders are required for the scintillation correction. This is to be expected as the defocus term (j = 4) of the high-altitude turbulence makes the largest contribution to the intensity fluctuations.

4.3 Photometry

Aperture photometry was performed on the target star in each subaperture and summed over all the subapertures. An annulus was used to measure the median background value for each subaperture to correct any field dependent background noise.

The crowding of WFS images resulted in several challenges in performing the photometry. First, the crowded field severely limited the size of the aperture that could be used to perform the photometry. In addition, measuring an accurate sky background was challenging due to nearby stars contaminating the annulus. To overcome this, a mask was applied to the annulus to try to avoid contamination by neighbouring stars skewing the measured background. A standard SNR versus aperture plot could not be used to determine the optimum aperture size to use since beyond a certain size, the aperture was contaminated with the light from the neighbouring stars. Hence, the size of aperture used had to be optimized based on the tomographic scintillation correction performance achieved. In addition, measuring the photometry with the subapertures also increased the total read-out noise. However, it is still an insignificant noise source in comparison to the scintillation noise as shown in Table 2.

The light curve obtained also contained slowly varying systematic trends. These are most likely due to changes in the airmass during the observation as we were observing at low elevations, as well as irregularities across the field. These could not be corrected via standard differential photometry due to the addition of random intensity fluctuations from the fainter comparison stars since the shot noise of the fainter comparison stars will dominate the measurement. Hence, a curve fitting algorithm was used to correct these low order systematic trends. A low-order polynomial was fit to the entire light curve and used to remove the systematic trends (Tamuz, Mazeh & Zucker 2005; Poddaný, Brát & Pejcha 2010). This is not ideal as it is difficult to distinguish between systematic trends and low order scintillation variations. However, the power spectrum of the low order systematic trends shown in Fig. 11 clearly shows that the power is in much lower frequencies than the frequency of the peak in the power of the scintillation. Thus, it is likely to be primarily low-order systematics that was corrected and not scintillation noise. In addition, this correction maximized the scintillation correction performance achieved.

Table 2. A table to compare the measured scintillation index and SNR with the expected scintillation index and SNR from the theory.

Exposure time	0.01 s	0.1 s	1 s
Expected scintillation index	1.9×10^{-5}	4.4×10^{-5}	4.4×10^{-6}
Average measured scintillation index	3.7×10^{-5}	4.2×10^{-5}	7.6×10^{-6}
Average measured scintillation rms	6.1×10^{-3}	6.5×10^{-3}	2.8×10^{-3}
Expected shot noise	4.7×10^{-4}	2.1×10^{-4}	6.0×10^{-5}
Read-out noise	6.2×10^{-5}	1.2×10^{-5}	1.2×10^{-6}

The expected scintillation index was estimated using the median of the measured SCIDAR turbulence profiles in equations (2) and (3).

As can be seen in Table 2, the average measured scintillation index is close to the expected scintillation index for the turbulence profile for the 0.1 s data. In addition, the measured scintillation noise far exceeds the expected shot noise and read noise, and thus we can be confident that the observations are limited by scintillation noise.

4.4 Turbulence profiles

To perform the tomography, the turbulent layer heights and relative strengths must be known. The turbulence profile is required to produce the projection matrices and the Zernike–Kolmogorov turbulence covariance matrix in the tomographic reconstruction matrix given in Section 2.2.

The median SCIDAR data taken 8 min before the start of the WFS run were used to estimate the turbulence profile above the telescope during the WFS observations. The median SCIDAR profile was then grouped into layers using the optimal grouping algorithm. This grouping method was selected as it was found to be optimum in terms of tomographic performance (Saxenhuber et al. 2017).

Fig. 8 shows the turbulence profiles measured on the night beginning 19th of September, 2021. The turbulence profiles observed at 4 am in observation period A, have a strong layer at the ground and a strong layer around 12 km but with many weaker layers in between. After 5 am, in observing period B, the strength of the high-altitude layer has increased and there are clearly two dominant layers, one at the ground and one at 12 km. Hence, in this paper, we focus on the WFS data collected from 5:30 am onward, where the profile is dominated by two strong layers and thus the tomographic reconstruction is simplified.

It should be noted that the turbulence conditions were not optimal for this demonstration. Whilst there is a dominant turbulent layer at 12 km, it does not produce strong scintillation due to its low C_n^2 value

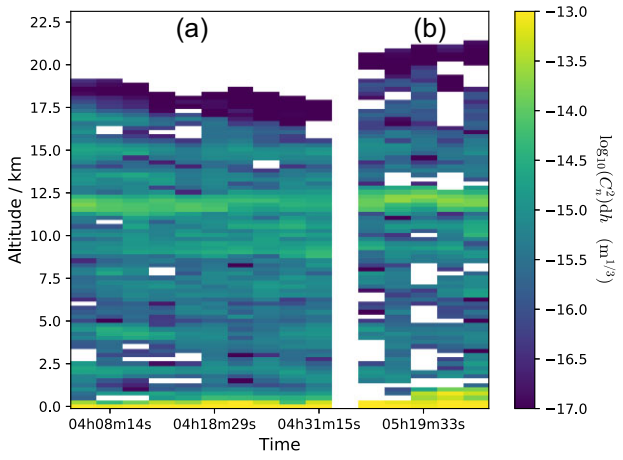

Figure 8. The turbulence profiles measured over 1.5 h of the night of the 19th of September. The observations are split into observing period A and B with a gap between the observations plotted. A strong turbulent layer is seen at the ground and at 12 km.

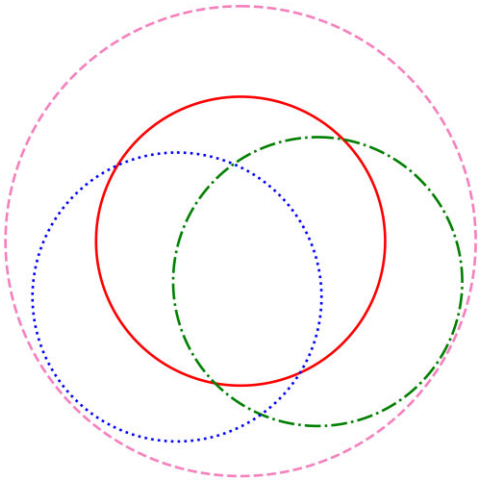

Figure 9. The overlap in WFS measurements for the three stars used in the tomographic reconstruction at 12 km. The target star, Orionis C, is placed in the centre of the meta-pupil and is shown in red, with Orionis D in green dash–dotted, and Orionis A in blue dotted.

of 5.9×10^{-14}. In addition, the profile is heavily dominated by the strong ground layer and the substantial dome seeing.

Fig. 9 shows there is significant overlap between the WFS measurements at the 12 km layer and hence good sampling of this dominant layer for the tomographic reconstruction is achieved.

4.5 Tomographic reconstruction

The tomographic reconstruction matrix, given in equation (8), was produced using the median five layer turbulence profile measured for the five profiles measured between 5:14 and 5:24 am and the geometry of the Orion Trapezium Cluster. Five layers were used in the reconstruction matrix as no benefit was found in using more layers. A reconstruction matrix was produced for each data packet using the optimal number of Zernike modes.

The reconstruction matrix was then applied to the measured Zernike coefficients for all three of the stars to produce an estimate for the phase aberrations at each of the five altitudes. A PYTHON package, AOTOOLS (Townson et al. 2019), was used to Fresnel propagate the reconstructed high layer phase aberrations metapupils to produce an estimate for the scintillation intensity fluctuation pattern at the ground. The telescope pupil was then cut out from the scintillation pattern metapupil (thus avoiding diffraction rings at the edge) and summed to estimate the intensity. This is then repeated for each frame to produce a temporal estimate of the intensity variance. For each data packet, we compute $C_{\rm scint}$ and r.

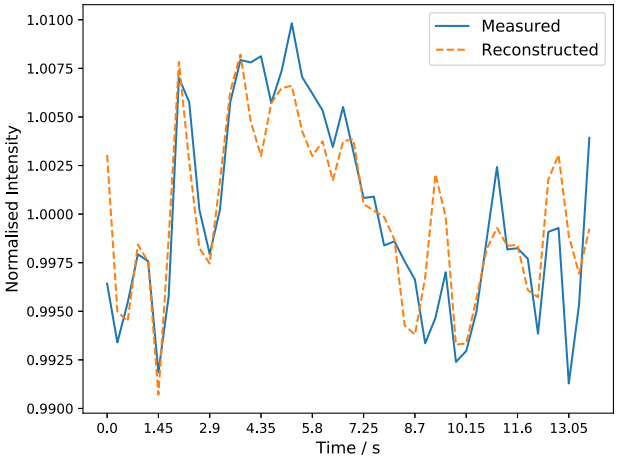

Figure 10. The measured normalized intensity and the normalized tomographically reconstructed intensity for the best performing 0.1 s data packet. The intensity was temporally binned by a factor of 2.

5 ON-SKY RESULTS

5.1 Example light curve

We have chosen to temporally bin our light curves by a factor of 2 in order to remove some of the high-frequency noise such that the correlation can be more clearly seen. Hence, the effective exposure times used are 0.02, 0.2, and 2 s.

Fig. 10 shows the measured normalized intensity and the reconstructed normalized intensity for the best performing 0.2 s data packet. This data packet has an SNR of 197 and a scintillation rms noise of 5.1×10^{-3}. For a star of magnitude 5.13 in the V band and for a 0.2 s exposure time for our instrument, we expect the shot rms noise of 1.6×10^{-4}. Hence, we can be confident that the overall SNR is dominated by scintillation.

The correlation coefficient between the measured and reconstructed intensities of this data packet is 0.86. The strong correlation between the measured and reconstructed light curves shows that the tomographic reconstruction is correctly estimating the low frequency intensity variations. Normalizing the measured photometry of this data packet with the reconstructed intensity reduced the scintillation index by a factor of 3.41, corresponding to a reduction in the scintillation rms noise by a factor of 1.85.

5.2 Power spectrum

Fig. 11 shows the average power spectra of the uncorrected and corrected light curves for the 0.1 s data packets for which a correction of at least 2 in the variance was achieved. The power at low frequencies has been significantly reduced in the corrected light curve. In addition, the power spectra for the measured defocus Zernike term of the high altitude turbulent layer at 12 km is also

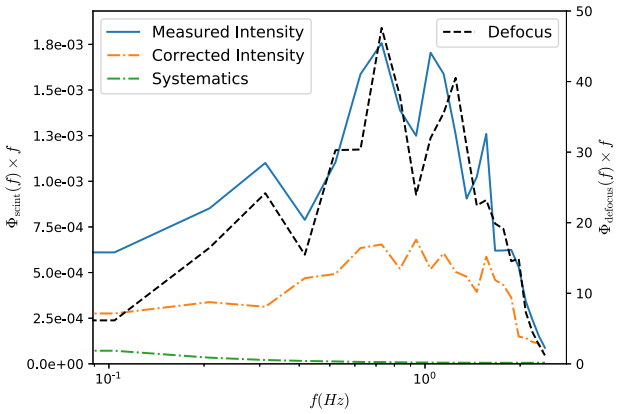

Figure 11. The average power spectra for the measured and corrected light curves is plotted using the left y-axis. The power spectrum for the measured systematic trends is also plotted. The power spectrum for the defocus Zernike mode measured for the 12 km turbulent layer is also plotted using the right y-axis.

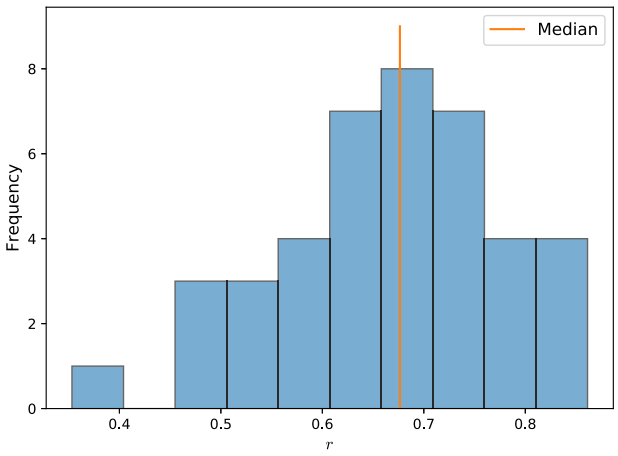

Figure 12. A histogram of the measured correlation coefficient between the measured intensity and tomographically reconstructed intensity. The median of the measured correlations is also plotted.

plotted. The shape of the power spectra of the measured intensity strongly resembles the power of the high altitude defocus Zernike term. This is discussed further in Section 5.4. Since there is no significant power above a few hertz, longer exposures can be used.

Since this on-sky proof of concept experiment has several limitations, the fact that such high correlation has been measured and that an average correction in the scintillation variance of ∼2 has been achieved, demonstrates the potential of the correction technique. We expect that with a full tomographic WFS system substantially greater scintillation noise correction would be achieved.

5.3 Performance metrics results

Fig. 12 shows a histogram of the measured correlation coefficient. The median correlation coefficient that was measured for all the data packets was 0.67 with a standard deviation of 0.11. The maximum correlation coefficient recorded was 0.86. These high correlations show that the tomography is correctly estimating the phase aberrations of the high-altitude layers and thus the scintillation

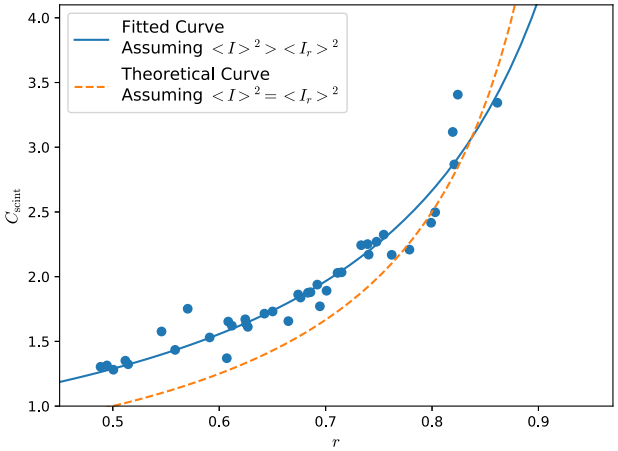

Figure 13. The measured correlation coefficient as a function of the measured Scintillation correction Factor with the theoretical curve for $\langle I \rangle^2 = \langle I_r \rangle^2$ and the fitted curve where $\langle I \rangle^2 > \langle I_r \rangle^2$.

pattern. To achieve any correction in the scintillation, a correlation coefficient of more than 0.5 is needed, which we achieve 88 per cent of the time.

Fig. 13 demonstrates the relationship between the correlation measured and the scintillation correction performance. The theoretical curve from equation (14), which assumes $\langle I \rangle^2 = \langle I_r \rangle^2$, is plotted in orange. The measured performance, with a fitted curve in blue where $\langle I \rangle^2 > \langle I_r \rangle^2$ in equation (13), achieves slightly higher performance at low correlations. This is likely favoured in the optimization of the data reduction parameters due to the presence of noise. It is also likely there are small scaling errors in the Fresnel propagation due to the limited knowledge of the true turbulence profile for each data packet.

Assuming $\langle I \rangle^2 = \langle I_r \rangle^2$, to halve the scintillation index, a correlation coefficient of at least 0.75 is needed. A scintillation correction factor of 2 or more was achieved for 35 per cent of the 0.2 s data packets.

There is a considerable scatter in the correlation coefficient measured. Simulations show that some statistical scatter is to be expected for measurements of short data packets. However, the observed scatter is much larger than would be expected. This may be explained by variations in the turbulence profile from packet to packet.

5.4 Exposure time

The correction performance that is achieved depends strongly on the exposure time that is used. This may be understood by considering the power spectra of the Zernike focal modes. The defocus term of the high-altitude turbulence makes the largest contribution to the intensity fluctuations. Fig. 11 shows the measured power spectrum of the high altitude defocus Zernike term.

The frequency corresponding to the peak in this power spectrum depends on the wind speed of the high-altitude layer and the size of the telescope aperture. If the exposure time is short, then the power is dominated by shot noise and thus low correction is achieved. If however a long exposure time is used then only the power in the low-frequency tail is measured and corrected, and hence a lower correction factor is achieved.

Hence, an optimum exposure time exists, for a given aperture size and high layer wind speed, where the scintillation correction factor will be maximized. Since the location of the peak scales with aperture

Table 3. The measured average and peak C_{scint} for each exposure time.

Exposure time	0.02 s	0.2 s	2 s
Average C_{scint}	1.35 ± 0.03	1.92 ± 0.08	1.48 ± 0.15
Peak C_{scint}	1.54	3.41	3.53

size, a larger aperture will have a peak at a lower frequency and thus a longer exposure time.

Table. 3 shows the average scintillation correction factor and peak correction factor measured as a function of the exposure time used. The 0.2 s data results in the largest correction factor. This result agrees with our findings from numerical simulation.

The 0.02 s data has the lowest correction factor whilst the 2 s data still achieves good performance. This demonstrates that relatively long exposures can be used to perform tomographic reconstruction in this way. Hence, exposure times and frame rates can be used which are closer to those typically used for time-resolved photometry rather than AO correction.

5.5 Expected performance simulation

A numerical simulation was produced to determine the expected scintillation correction performance for the measured SCIDAR profiles in observing period B in Fig. 8. This was used to determine whether the correction achieved is close to what could be expected for such turbulence profiles and, in particular, whether the correction is limited due to the lack of simultaneous profiling.

The profiles given in Section 4.4 were used to estimate the expected performance. Each profile was grouped into fifteen layers using the optimal grouping technique. These profiles were used to simulate a Monte Carlo phasescreen representation of the atmosphere. The simulation assumes that the WFS can measure the atmospheric Zernike terms perfectly with only shot noise added to the WFS data. In addition, the simulated target light curve is completely scintillation limited with no other noise sources. The simulation also assumes perfect measurement of the turbulence profile.

The tomographic reconstruction was then performed on each profile using a five-layer estimate for the turbulence profile. Five layers were chosen to correct the 15 layer profiles in simulation in order to include some tomographic model error in the simulation and thus simulate a more realistic performance that can be achieved. In practice, C_n^2 is a continuous function which we approximate with a discrete number of layers, N, in the reconstruction matrix, and thus there will always be some model error. We find that with $N > 5$ layers, there is little difference in the performance and therefore the model error is small.

The median five layer profile observed between 5:14 am and 5:24 am in observing period A was also used to correct the simulated intensity. This was to test the performance of the median profile over the five profiles measured and to justify its use for the data collected as little change in the performance is seen. In addition, the median five layer profile measured by the SCIDAR run between 4:05 am and 4:30 am in observing period B was used to determine how significantly the profile has changed over the 45 min between the two SCIDAR runs.

As can be seen in Fig. 14, the measured performance varies from profile to profile. The median profile in observing period B shows reasonable performance, whilst using the median profile in observing period A, measured 45 min prior, performs badly. This can be expected, as the profile has changed between the two runs as seen in Fig. 8. This demonstrates the necessity for regular profiling to perform accurate tomographic reconstruction.

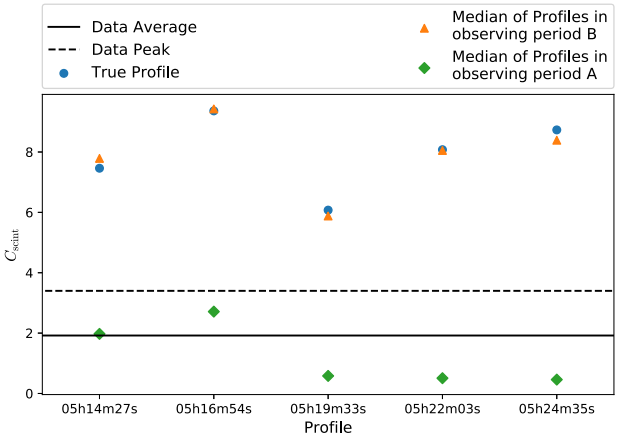

Figure 14. The measured scintillation correction factor in simulation for each turbulence profile. The performance is plotted for several reconstruction matrices using either the true turbulence profile, the median of the profiles measured in observing period A, and the median of the profiles measured in observing period B. The average and peak performance for the WFS data collected after 5:30 am is also plotted.

Comparing the scintillation correction performance obtained using the real data with the expected performance from the simulation of the SCIDAR profiles shows that the measured performance is lower. This is to be expected as the simulation assumes perfect measurement of the turbulence profile above the telescope as well as perfect photometry and Zernike wavefront sensing. Hence, the simulation provides an upper limit for the scintillation correction that can be expected.

The average and peak scintillation correction results for the data are on average better than those measured in simulation using the median profile in observing period A. This suggests that the turbulence profile has not changed significantly between the SCIDAR observing period B and the wavefront sensing. However, it may have still changed enough to reduce the correction performance. We expect that simultaneous turbulence profiling would provide improved performance, and would the reconstruction matrix to be updated as regularly as is required.

6 IMPLICATIONS FOR FACILITY IMPLEMENTATION

In this section, results from simulations are presented to demonstrate the expected scintillation correction performance that can be achieved on a full tomographic AO system.

6.1 Updating the tomographic algorithm

Based on the on-sky results, it is important to assess how regularly the tomographic reconstruction matrix needs to be updated.

Farley et al. (2020) explore how regularly the tomographic reconstruction matrix must be updated for AO on the ELT, with results suggesting that 20 min is optimal. The same turbulence profile data have been used to see how the scintillation correction performance changes with time interval.

We expect that for scintillation correction, the turbulence profile used will need to be updated more regularly than for AO correction. This is because for scintillation correction, not only is knowledge of

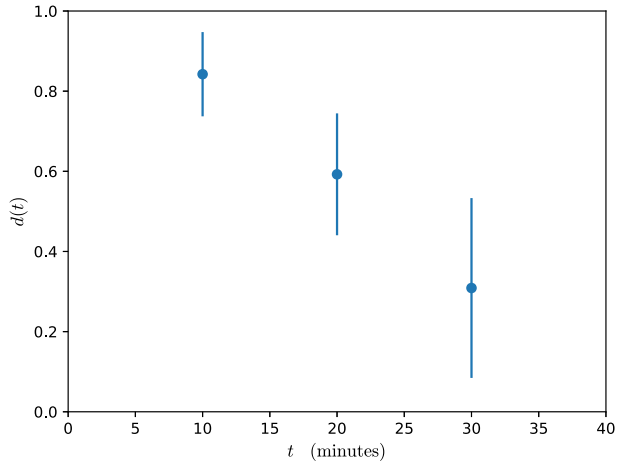

Figure 15. The fractional reduction in the scintillation correction factor between $t = t$ and $t = 0$ as a function of time. The error bars are the standard error of all the profiles used.

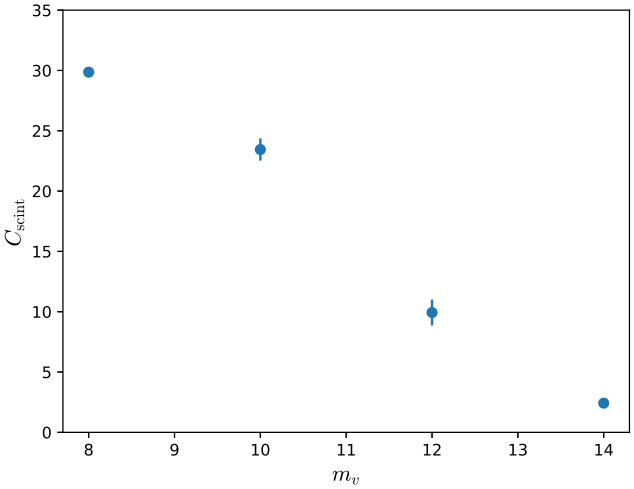

Figure 16. The scintillation correction factor against the magnitude of the reference stars used to perform the tomography.

the turbulence profile necessary to perform the tomography, but it is also needed to perform the Fresnel propagation. Hence, knowledge of the turbulence heights is vital.

A numerical simulation was performed using SCIDAR profiles measured in Paranal in 2018. The tomographic error performance using the Trapezium asterism was measured over time. The tomographic error was compared for a tomographic reconstruction matrix using the current $t = t$ profile and the $t = 0$ profile. Profiles where the change in the relative tomographic error was close to the median value were selected. These median profiles at time t were simulated using a Monte Carlo phase screen representation of the atmosphere and the scintillation correction was performed both with the $t = t$ profile and the $t = 0$ profile, where $t = 10$, 20, and 30 min.

To quantify the difference in the performance achieved, the fractional change in the scintillation correction factor between using the $t = t$ profile and the $t = 0$ profile in the tomographic reconstruction matrix was measured such that:

$$\mathrm{d}(t) = \frac{C_{\text{scint}}(t = 0)}{C_{\text{scint}}(t = t)}. \tag{15}$$

Fig. 15 shows d(t) as a function of time. The reduction in performance increases with the time interval. After 20 min, there is already a 40 per cent reduction in performance when the reconstruction matrix is not updated. This increases to 70 per cent after 30 min. It is clear that using the current profile results in optimum performance and therefore regular simultaneous turbulence profiling on the timecale of ∼10 min is required.

For the on-sky data presented in Section 5,there was a lag between the SCIDAR observation and the start of the WFS run of 8 min. In addition, the WFS data were collected over half an hour period. Hence, if we assume the profile changed by a median amount over this time, and that on average $t \approx 20$; then based on Fig. 15, the correction measured is ∼ 40 per cent smaller than what could be achieved with simultaneous profiling. Therefore, with simultaneous turbulence profiling, we could expect to have achieved an average C_{scint} of 3.2 and a peak of 5.7.

6.2 Sky coverage

Another key question is whether substantial sky coverage can be achieved for this technique using natural guide stars (NGS). For a large telescope, longer exposure times and larger asterisms can be used and hence a larger sky coverage might be expected.

To determine the sky coverage for a tomographic AO system on a large telescope a simulation for an 8 m class telescope was produced. 18 Paranal SCIDAR profiles, each with five layers was used. A configuration with a very bright scintillation limited target (V = 5) was chosen with 4 stars in a square with sides of 63 arcsec. The magnitude of the four stars was varied from 8 to 14. A one second exposure time and a 16 × 16 WFS was used for each guide star from which 100 Zernike modes (a more than sufficient number of modes, well within what could be reasonably measured) were used in the tomographic reconstruction. It was assumed the observation was near zenith. The scintillation correction factor was then plotted against the reference star magnitudes. The results of this simulation are shown in Fig. 16.

The scintillation correction factor reduces significantly as the reference stars used to perform the tomography get fainter. Hence, brighter stars (V ≤ 10) are required to accurately perform the tomography. As such, the expected sky coverage for an NGS tomographic system would be negligible, despite the fact that a longer exposure time and wider asterism are used. In addition, even if there were enough stars within the asterism required, the probability of it being in a suitable configuration would be small. Therefore, the use of LGS is required. The 4LGSF which have magnitudes $V \sim 8$ and therefore provide more than enough flux for this application. Fortunately, the newest large and extremely large telescopes will all be equipped with LGS facilities for tomographic AO and therefore this requirement will already be met.

6.3 Implementation on LGS AO facility

It is clear that this scintillation correction technique ideally needs to be performed on a large class telescope with a full tomographic AO system along with simultaneous turbulence profiling. As such a numerical simulation was performed to determine the level of scintillation correction that could be achieved for such a system.

Based on the results for the sky coverage, it is clear that an ideal application of this method requires an LGS facility. However, whilst LGS provide full sky coverage, there are several disadvantages to their use including the cone effect, the tip/tilt indetermination problem and spot elongation. As such, the 4LGSF on the VLT were

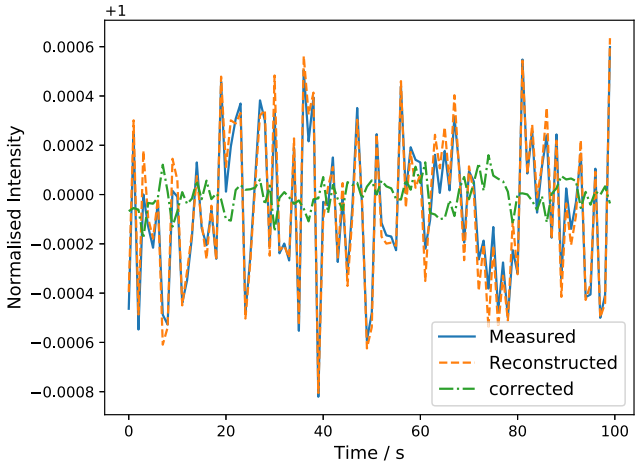

Figure 17. An example simulated light curve for the 4LGSF on the VLT. The measured normalized intensity, tomographically reconstructed normalized intensity, and corrected intensity are plotted.

simulated with these effects included to estimate the scintillation correction that can be achieved on a full tomographic AO system with LGS.

The cone effect was included by setting an LGS height of 90 km in the WFS measurements and in the reconstruction matrix as described by Rosensteiner & Ramlau (2013). The LGS spot elongation was included in the WFS noise model using the noise covariance matrix defined by Clare, Louarn & Béchet (2010). The tip/tilt indetermination was included in the simulation by excluding tip/tilt from the tomographic reconstruction matrix. It is expected that any differential tip/tilt between the LGS at the high-altitude layers are likely small as there is significant overlap in the WFS measurements. Hence, On-sky, the target NGS could be used to measure the tip/tilt. It is assumed that the height of the LGS is known and hence the remaining Zernike modes can be measured perfectly.

The VLT was simulated with the four LGS in a square with sides of 63 arcsec with a scintillation limited target star in the middle and it was assumed that the observation was near zenith. A one second exposure time was used and 100 Zernike modes were employed in the tomographic reconstruction. The expected shot noise for an $V =$ 8 mag LGS with a 16 × 16 WFS was added to the measured Zernike modes for each guide star. 18 turbulence profiles measured in Paranal (Farley et al. 2018) were used in simulation, each compressed to five layers, using an optimal grouping algorithm. A total data acquisition of 100 s was simulated for each turbulence profile.

Fig. 17 shows an example of the measured normalized intensity, reconstructed intensity, and corrected intensity for one of the turbulence profiles. The noise has been substantially reduced in the corrected light curve. The measured correlation between the measured and reconstructed intensity is 0.98 which results in a scintillation correction factor of 22 – a reduction in the scintillation rms noise by a factor of 4.7. It was found that on average for all the turbulence profiles, the scintillation rms noise was reduced by a factor of 4. This is slightly reduced from the factor of 5.5 ($C_{\rm scint} =$ 30) that was measured for the same configuration with $V = 8$ NGS in Fig. 16.

These simulations assume perfect knowledge of the turbulence profile and sets the number of reconstructed layers to the number of layers in the atmosphere. In addition, the WFS measurements are assumed to be entirely limited to shot noise. Therefore, these simulations give an upper limit of the performance that can be expected for an LGS facility.

Whilst a tomographic AO system will be operating at very high frame rates, we have demonstrated that the wavefront and the intensity temporally average in the same way. Hence, the reconstructed intensity can be temporally binned (so long as the scintillation remains the dominant noise source) to apply correction over longer exposures for the photometric data.

7 DISCUSSION AND CONCLUSIONS

High-precision ground-based photometry can be severely limited by atmospheric scintillation noise. The first ever on-sky demonstration of a scintillation correction technique has been presented. A simple proof-of-concept experiment observing the Orion Trapezium cluster using a single wavefront sensor and SCIDAR instrument on the Isaac Newton Telescope was performed. The results from this experiment have successfully proved the concept, although the correction achieved is relatively low. An average reduction in the scintillation rms noise by a factor of 1.39 was achieved for the 0.1 s data. However, the on-sky experiment has highlighted a number of ways in which the correction performance can be improved for a facility system.

It was found that the turbulence profiles measured with SCIDAR changed substantially between observations and using an out of date profile severely limits performance. We expect that the scintillation correction performance would be greatly improved if simultaneous turbulence profiling is available.

A separate turbulence profiler is not necessarily needed. We used a SCIDAR instrument on-sky to estimate the turbulence profile as we were using long exposure times; however, the profile could be obtained from the WFS telemetry data if high frame rates are used. On a full tomographic AO facility, bursts of WFS data at high frame rates could be measured and used to estimate the turbulence profile every ∼10–15 min. As such, this technique could be easily applied to any existing and future tomographic AO facilities without the need for any additional hardware.

Another significant limitation to this demonstration is that the photometry was performed using the WFS frames. The crowded field limited the photometric aperture size that could be used and the ability to measure an accurate sky background value. In addition, any long time-scale systematic trends in the photometry severely limit the scintillation correction performance that can be achieved. Differential photometry cannot be used to correct these trends as random noise from the comparison star is added during the calibration. As such, the systematic trends had to be removed using a simple polynomial curve fitting algorithm. Whilst this does a good job at removing low-order trends, any high order trend cannot be corrected this way as it is impossible to differentiate between scintillation noise and other noise sources.

Despite these limitations, we have measured strong correlation between the uncorrected and tomographically reconstructed intensities with a maximum correlation of 0.86 achieved. We expect that, with optimal instrumentation, this method would achieve substantial scintillation correction.

Results from simulation show that even for the largest telescopes, a significant sky coverage cannot be achieved using NGS. Hence, for most targets of interest, LGS are required. Simulations of the 4LGSF facility on the VLT show that high scintillation correction factors of ∼25 could be achieved.

ACKNOWLEDGEMENTS

This work was supported by the Science and Technology Facilities Council [ST/N50404X/1] and [ST/T506047/1]. The authors would like to thank the Isaac Newton Group (ING) for the use of the Isaac Newton Telescope. We would also like to thank the anonymous reviewer for their insightful comments and suggestions.

KH and JO acknowledge support from UK Research and Innovation (Future Leaders Fellowship MR/S035338/1).

This research made use of PYTHON including NUMPY and SCIPY (van der Walt, Colbert & Varoquaux 2011), MATPLOTLIB (Hunter 2007), ASTROPY, a community-developed core PYTHON package for Astronomy (The ASTROPY Collaboration 2013) the PYTHON AO utility library AOTOOLS (Townson et al. 2019).

DATA AVAILABILITY

The data underlying this article will be shared on reasonable request to the corresponding author.

REFERENCES

Beckers J. M., 1988, in Ulrich M-H, ed., Very Large Telescopes and Their Instrumentation, ESO Conference and Workshop Proceedings. European Southern Observatory (ESO), Garching, p. 693
Ciliegi P. et al., 2021, Messenger, 182, 13
Clare R. M., Louarn M. L., Béchet C., 2010, Appl. Opt., 49, G27
Dai G., 1996, J. Opt. Soc. Am. A, 13, 1218
Dainty J. C., Levine B. M., Brames B. J., O'Donnell K. A., 1982, Appl. Opt., 21, 1196
Dravins D., Lindegren L., Mezey E., Young A. T., 1997a, Publ. Astron. Soc. Pac., 109, 173
Dravins D., Lindegren L., Mezey E., Young A. T., 1997b, Publ. Astron. Soc. Pac., 109, 725
Dravins D., Lindegren L., Mezey E., Young A., 1998, Publ. Astron. Soc. Pac., 110, 610
Farley O. J. D., Osborn J., Morris T., Sarazin M., Butterley T., Townson M. J., Jia P., Wilson R. W., 2018, MNRAS, 481, 4030
Farley O. J. D., Osborn J., Morris T., Fusco T., Neichel B., Correia C., Wilson R. W., 2020, MNRAS, 494, 2773
Föhring D., Wilson R., Osborn J., Dhillon V., 2015, J. Phys.: Conf. Ser., 595, 012010
Fusco T., Conan J.-M., Rousset G., Mugnier L. M., Michau V., 2001, J. Opt. Soc. Am. A, 18, 2527
Hunter J. D., 2007, Comput. Sci. Eng., 9, 90
Kornilov V., 2012, MNRAS, 426, 647
Madhusudhan N., Knutson H., Fortney J. J., Barman T., 2014, in Protostars and Planets VI. Univ. Arizona Press, Arizona, p. 739
Marchetti E. et al., 2007, Messenger, 129, 8
Mikesell A. H., 1955, Publ. U.S. Nav. Obs. Second Ser., 17, 139
Noll R. J., 1976, J. Opt. Soc. Am., 66, 207
Osborn J., 2014, MNRAS, 446, 1305
Osborn J., Wilson R., Butterley T., Shepherd H., Sarazin M., 2010, MNRAS, 406, 1405
Osborn J., Wilson R. W., Dhillon V. S., Avila R., Love G. D., 2011, MNRAS, 411, 1223
Osborn J., Föhring D., Dhillon V. S., Wilson R. W., 2015, MNRAS, 452, 1707
Poddaný S., Brát L., Pejcha O., 2010, New Astron., 15, 297
Ragazzoni R., Marchetti E., Rigaut F., 1999, A&A, 342, L53
Reeves A., 2016, in Marchetti E., Close L. M., Véran J.-P., eds, Proc. SPIE Conf. Ser. Vol.9909, Adaptive Optics Systems V. SPIE, Bellingham, p. 2173
Rigaut F., Gendron E., 1992, A&A, 261, 677
Roddier F., 1981, Progress in Optics, 19, North-Holland Publishing Co., Amsterdam, p. 281
Rosensteiner M., Ramlau R., 2013, J. Opt. Soc. Am. A, 30, 1680
Ryan P., Sandler D., 1998, Publ. Astron. Soc. Pac., 110, 1235
Sasiela R. J., 2012, Electromagnetic Wave Propagation in Turbulence: Evaluation and Application of Mellin Transforms, Vol. 18. Springer Science & Business Media, Berlin, Heidelberg
Saxenhuber D., Auzinger G., Louarn M. L., Helin T., 2017, Appl. Opt., 56, 2621
Schmidt J. D., 2010, Numerial Simulation of Optical Wave Propagation with Examples in MATLAB. SPIE, Bellingham
Shepherd H. W., Osborn J., Wilson R. W., Butterley T., Avila R., Dhillon V. S., Morris T. J., 2013, MNRAS, 437, 3568
Tamuz O., Mazeh T., Zucker S., 2005, MNRAS, 356, 1466
Tatarski V. I., 1967, Wave propagation in a turbulent medium / V. I, Tatarski; translated from the Russian by R. A. Silverman. Dover, New York
Taylor G. I., 1938, Proc. R. Soc. A, 164, 476
Thatte N. et al., 2010, in McLean I. S., Ramsay S. K., Takami H., eds, Proc. SPIE Conf. Ser. Vol. 7735, Ground-based and Airborne Instrumentation for Astronomy III. SPIE, Bellingham, p. 77352I
The Astropy Collaboration, 2013, A&A, 558, A33
Townson M. J., Farley O. J. D., de Xivry G. O., Osborn J., Reeves A. P., 2019, Opt. Express, 27, 31316
van der Walt S., Colbert S. C., Varoquaux G., 2011, Comput. Sci. Eng., 13, 22
Wilson R. W., Jenkins C. R., 1996, MNRAS, 278, 39
Young A. T., 1969, Appl. Opt., 8, 869

This paper has been typeset from a TEX/LATEX file prepared by the author.